

Evidence of Spin-Valley Coupling in Dirac Material BaMnBi₂ Probed by Quantum Hall Effect and Nonlinear Hall Effect

Subin Mali¹, Yingdong Guan¹, Lujin Min^{1,2}, David Graf³, and Zhiqiang Mao^{1,2*}

¹Department of Physics, Pennsylvania State University, University Park, PA 16802, USA

²Department of Materials Science and Engineering, The Pennsylvania State University, University Park, PA 16802, USA

³National High Magnetic Field Lab, Tallahassee, Florida 32310, USA

ABSTRACT

Valleytronics is a rapidly advancing field that explores the use of the valley degree of freedom in electronic systems to encode and process information. It relies on electronic states with spin-valley locking, first predicted and observed in monolayer transition metal dichalcogenides like MoS₂. However, very few bulk materials have been reported to host spin-valley locked electronic states. In this work, we present experimental evidence for a predicted, unique spin-valley locked electronic state generated by the Bi zig-zag chains in the layered compound BaMnBi₂. We observed remarkable quantum transport properties in this material, including stacked quantum Hall effect (QHE) and nonlinear Hall effect (NLHE). From the analysis of the QHE, we identified a spin-valley degeneracy of 4, while the NLHE provides supporting evidence for the anticipated valley-contrasted Berry curvature—a typical signature of a spin-valley locked state. This spin-valley locked state contrasts with that observed in the sister compound BaMnSb₂, where the degeneracy is 2. This difference arises from significant variations in their orthorhombic structures and spin-orbital coupling. These findings not only set up a new platform for exploring coupled spin-valley physics in bulk materials but also underscores its potential for valleytronic device applications.

*Email: zim1@psu.edu

I. INTRODUCTION

Non-centrosymmetric materials with strong spin-orbit coupling (SOC) often display electronic states characterized by spin splitting of energy bands. When the valley degree of freedom is incorporated into these materials, the spin and valley degrees of freedom become coupled (also termed spin-valley locking), creating unique electronic states. This coupling allows for the control and manipulation of the valley degree of freedom [1] using electric fields [2], magnetic fields [3], or light [4]. These unconventional electronic states hold great promise for a wide range of potential applications, including valleytronic logic gates and valley-based memory devices [5,6].

The spin-valley locked state was first predicted in MoS₂ monolayers [1] and later demonstrated experimentally through optical helicity-controlled valley polarization [7], optically driven valley polarization [8], and spin-pseudospin spectroscopy [9,10]. The inversion symmetry is broken in monolayers, and the conduction and valence band edges are located at the corners (K points) of the 2D hexagonal Brillouin zone. The combination of strong SOC and inversion symmetry breaking in these materials enables spin splitting at K and K' valleys with opposite spin orientation, leading to the valley dependent spin polarization, i.e. spin-valley locking. Spin-valley coupling in TMDCs has given rise to various interesting phenomena, such as valley-dependent circular dichroic photoluminescence [8,11,12], nonreciprocal charge transport [13], photo-induced charge Hall effect [1], valley Hall effect [14], and exciton Hall effect [15] in the absence of an external magnetic field. In the bulk form of TMDCs, there have been two reported examples that demonstrate spin-valley locking, namely 3R-MoS₂ [16] and 2H-NbSe₂ [17]. Besides TMDCs, layered polar Dirac material BaMnSb₂ has been identified as the only known bulk material exhibiting spin-valley locking beyond TMDCs [18]. In BaMnSb₂, the Sb zig-zag chain layers break in-plane inversion symmetry and combined with the strong SOC from the Sb atoms, two Dirac valleys with valley-contrasting out-of-plane spin polarizations are formed around the X point. This was revealed through first-principles calculations, angle-resolved photoemission spectroscopy (ARPES), and quantum Hall measurements [18–20].

To further understand coupled spin and valley physics and explore valleytronic and optoelectronic applications of spin-valley locked states, it is crucial to find various spin-valley locked states in more bulk materials. Despite the availability of numerous materials with inversion symmetry breaking and strong SOC, the limited number of known candidates underscores the challenge in identifying new materials with this unique property. Recently, Kondo et al. [21] used crystallographic analysis, first-principles calculations, and quantum oscillation measurements to investigate BaMnBi_2 , a sister compound of BaMnSb_2 . Their work predicted the existence of multiple pairs of Dirac valleys featuring valley dependent spin polarization and reported that, similar to BaMnSb_2 , BaMnBi_2 also exhibits a polar orthorhombic structure with the space group $Imm2$ (No. 44) [21]. Its orthorhombic distortion leads Bi to form zigzag chain layer which hosts Dirac fermions and is sandwiched between the insulating Ba^{2+} - Mn^{2+} - Bi^{3-} - Ba^{2+} slabs (Fig. 1a). However, BaMnBi_2 exhibits a slightly contracted c -axis, but significantly reduced orthorhombicity compared to BaMnSb_2 [21]. These structure characteristics, combined with stronger SOC of Bi, lead BaMnBi_2 to possess a spin-valley locked Dirac state distinct from that of BaMnSb_2 . BaMnSb_2 exhibits a single pair of valleys with spin-valley locking near the X-point on the zone boundary (Fig. 1b, left panel). In contrast, the spin-valley locked state in BaMnBi_2 is reported to possess four and two spin-polarized valleys near the X and Y points, respectively, as well as four additional valleys near the midpoint of the Γ -M line (Fig. 1b, right panel) [21]. DFT calculations and Shubnikov-de Haas (SdH) oscillations reported in Ref. [21] provide strong evidence for spin-split bands in BaMnBi_2 . While these results represent a significant advance in understanding its electronic structure, direct experimental demonstration of topological quantum transport arising from this unique spin-valley-locked state, as well as identification of the spin-valley degeneracy, has yet to be achieved.

Here we report on quantum transport properties of BaMnBi_2 . Through systematic measurements conducted on this material, we not only observed a stacked quantum Hall effect (QHE) but also detected an intrinsic nonlinear Hall effect (NLHE) [22]. The QHE analysis revealed a spin-valley degeneracy of 4, indicating the presence of two pairs of spin-valley locked Dirac cones near the Fermi level in BaMnBi_2 , contrasted with the spin-valley locked state with a degeneracy of 2 observed in BaMnSb_2 . Moreover, the

observation of intrinsic NLHE in bulk BaMnBi₂ single crystals suggests the existence of a Berry curvature dipole [23,24] in its band structure, providing strong supporting evidence for the expected valley-contrasted Berry curvature in a spin-valley locked state. These findings position BaMnBi₂ as a promising candidate for the further exploration of coupled spin-valley physics in bulk materials.

II. EXPERIMENTAL DETAILS AND METHODS

The BaMnBi₂ crystals used in this study were grown using the Bi-flux method. The starting materials of Ba, Mn, and Bi metals were mixed in a small alumina crucible at a ratio of Ba:Mn:Bi = 1: 1: 4 or 1: 1: 5 and then sealed in an evacuated quartz tube. The ampoule was heated to 1000 °C and held at that temperature for 1 day, followed by a slow cooling process at a rate of 2 °C/h to 400 °C. The ampoule was inverted, and the flux and single crystals were separated by a centrifuge. Plate-like single crystals as large as a few millimeters were obtained. X-ray diffraction (XRD) was utilized to analyze and confirm the crystal structure of the synthesized samples. Supplementary Fig. 3 presents the XRD pattern measured on the (001) plane. The sharp (00l) peaks demonstrate good crystalline quality of the grown crystals.

BaMnBi₂ crystals exhibit reduced air stability compared to BaMnSb₂ crystals. Hence, the crystals were handled carefully to minimize degradation and ensure measurement reliability. Crystals were stored in an argon-filled glovebox, and samples were prepared and measured within one hour of exposure to atmosphere. For high-field measurements, GE varnish was applied over the samples to encapsulate the sample after electrical contacts were made using silver epoxy, which significantly improved the sample's air stability during measurements at the magnet lab.

High-field transport measurements were performed at the National High Magnetic Field Laboratory (NHMFL) DC-field facility in Tallahassee, FL, USA. The data presented in this paper for magnetoresistivity and Hall resistivity were obtained by symmetrizing and anti-symmetrizing the longitudinal and transverse Hall resistivity measurements taken at positive and negative magnetic fields, respectively. Nonlinear transport measurements were performed using a lock-in technique with a Quantum Design Physical

Property Measurement System (PPMS). A Keithley 6221 precision AC/DC current source provided the driving current. AC and DC voltages were measured using the Stanford Research SR860 lock-in amplifier.

III. RESULTS AND DISCUSSION

A. Quantum Hall effect

Figure 1c shows a representative crystal image captured with a polarized light microscope, clearly revealing strip-like domains. This observation indicates that the structure of our BaMnBi₂ crystals is orthorhombic, as recently determined by Kondo et al. [21], rather than the previously reported tetragonal structure [25]. From the domain wall orientation, the crystallographic *a* (or *b*) axis can be determined. Specifically, the *a*- (or *b*-) axis forms a 45° angle relative to the domain wall, and the *a/b*-axis is rotated by 90° across the domain wall, as illustrated in Fig. 1c. Due to the minimal difference between the lattice parameters of *a* and *b*, distinguishing them using a Laue pattern is impossible. Since the orthorhombic distortion in BaMnBi₂ is much smaller than in BaMnSb₂, it leads to a unique spin-valley locked state, distinct from that in BaMnSb₂, as illustrated in Fig. 1b. Given that our prior work demonstrated the efficacy of electric transport measurements in probing spin-valley degeneracy via the QHE [18] and valley-contrasted Berry curvature via the NLHE [26] in BaMnSb₂, we conducted similar transport studies on BaMnBi₂. Our aim was to reveal transport signatures of spin-valley locked Dirac fermions in BaMnBi₂ by investigating its potential QHE and NLHE.

We performed magnetoresistivity measurements on two representative samples of BaMnBi₂ with the electric current applied to the *a/b*-axis (Sample #A) and *c*-axis (Sample #C) respectively, under high magnetic fields of up to approximately 35T (see the insets to Fig. 1d-f for the experimental configurations). Figure 1d-f illustrates the magnetic field dependence of Hall resistivity (ρ_{xy}), in-plane resistivity (ρ_{xx}), and out-of-plane resistivity (ρ_{zz}) measured at a temperature of 1.4 K respectively. All these data exhibit SdH oscillations starting from around 5T. It is evident from Fig. 1d-e that when ρ_{xx} reaches minima at about 10 and 23T, ρ_{xy} displays distinct plateau features as marked by the horizontal/vertical dashed lines, providing an implication of bulk QHE in BaMnBi₂ (Note that the Hall resistivity data in Fig. 1d is presented with $-\rho_{xy}$

for better visualizing the plateau characteristics). Furthermore, we also note that the SdH oscillations of ρ_{zz} are out-of-phase with those of ρ_{xx} . A similar phenomenon was also observed in BaMnSb₂ and is attributed to distinct transport mechanisms between the in-plane and out-of-plane directions. Since BaMnSb₂ possesses a quasi-two-dimensional (2D) electronic band structure, its interlayer transport occurs via the tunneling process, in contrast with in-plane band transport [18]. According to the Lifshitz-Kosevich (LK) theory [27,28], ρ_{xx} exhibits a minimum when the density of state at the Fermi level E_f [DOS(E_f)] reaches a minimum. The minimal DOS(E_f) leads to a minimal interlayer tunneling conductivity such that ρ_{zz} exhibits a maximum at minimal ρ_{xx} . Given that BaMnBi₂ shares a similar layered structure with BaMnSb₂, the electronic band structure of BaMnBi₂ should also be quasi-2D, which was indeed demonstrated in prior work [25]. Therefore, the interlayer tunneling mechanism should also apply to BaMnBi₂ and can explain why its ρ_{zz} and ρ_{xx} exhibits out-of-phase SdH quantum oscillations. This is in line with the large resistivity ratio between the out-of-plane and in-plane direction probed in BaMnBi₂ ($\rho_{zz}/\rho_{xx} \sim 115 - 140$ at 1.4 K, refer to Supplementary Figure 2 [29]) and further implies that the weak interlayer coupling may lead to the presence of stacked QHE in BaMnBi₂ as seen in BaMnSb₂ [18]. On the other hand, we note that ρ_{zz} exhibits metallic-like temperature dependence (Supplementary Figure 2). This behavior is not necessarily incompatible with a tunneling-dominated transport mechanism. In general, when the tunneling barrier is low and transmission is coherent, the tunneling conductance can remain sufficiently high such that the overall temperature dependence of the junction resistance appears metallic-like, as observed, for example, in c-axis junctions prepared by cleaving Ru-containing Sr₂RuO₄ single crystals [30]. The metallic-like c-axis behavior observed in both BaMnSb₂ and BaMnBi₂ may arise from a similar scenario.

To find further evidence of the possible QHE in BaMnBi₂, we conducted not only magnetic field sweep measurements of ρ_{xy} (Fig. 2a), ρ_{xx} (Fig. 2e) and ρ_{zz} (Fig. 2i) under various field orientations at a fixed temperature (1.4 K), but also field sweep measurements of ρ_{xy} (Fig. 2c), ρ_{xx} (Fig. 2g), ρ_{zz} (Fig. 2k) at various temperatures under the magnetic field perpendicular to the *ab*-plane. Figure 2a illustrates that the values of the ρ_{xy} plateaus remain constant regardless of the field orientation angle θ (see the inset to Fig. 2a), as

highlighted by the two horizontal dashed lines. This suggests that the Hall plateaus depend solely on the effective field, i.e. the field component perpendicular to the *ab*-plane ($B_{\perp} = B\cos(\theta)$). This feature is further illustrated in Fig. 2b which shows the angular dependence of ρ_{xy} at 10 T and 23 T where the Hall plateaus were observed. As depicted, the ρ_{xy} value at 10 T remains nearly constant as θ increases from 0 to 40°, but decreases significantly for $\theta > 40^{\circ}$. At 23 T, ρ_{xy} exhibits a similar angular dependence, with a slight decrease from 0 to 40° attributed to the valley splitting, as explained below. These results contrast sharply with the expected angular dependence of Hall resistivity for normal conductors where $\rho_{xy} \propto B\cos\theta$ (indicated by the dashed lines in Fig. 2b). However, they can be well understood in terms of the QHE. The angle-independent ρ_{xy} at 10 T and 23 T within the $0 \leq \theta < 40^{\circ}$ range suggests that the Hall resistivity quantization remains unchanged with the field rotation within this angle range. The angular dependences of $\rho_{xx}(B)$ (Fig. 2e-f) and $\rho_{zz}(B)$ (Fig. 2i-j) are in line with this argument. Specifically, when $\rho_{xy}(B)$ exhibits a plateau (Fig. 2a), $\rho_{xx}(B)$ and $\rho_{zz}(B)$ consistently shows a minimum and a maximum, respectively, regardless of θ (Fig. 2e & 2i). Moreover, as shown in Fig. 2f & 2j, the ρ_{xx} and ρ_{zz} values at 10 T display minimal variation with θ in the $0 \leq \theta < 40^{\circ}$ range where ρ_{xy} remains constant, but show significant variations for $\theta > 40^{\circ}$, where ρ_{xy} decreases noticeably. These unusual angular dependences of ρ_{xx} and ρ_{zz} apparently do not follow the $\cos^2(\theta)$ dependence expected for trivial metals (indicated by the dashed lines in Fig. 2f & 2j) but align with the quantum Hall scenario. The large variation of the ρ_{xx} and ρ_{zz} values at 23 T within the $0 \leq \theta < 40^{\circ}$ range is associated with valley splitting, as will be explained below.

The indication of QHE in BaMnBi₂ was also revealed through temperature dependent measurements of $\rho_{xy}(B)$ (Fig. 2c), $\rho_{xx}(B)$ (Fig. 2g) and $\rho_{zz}(B)$ (Fig. 2k). In Fig 2c, the ρ_{xy} plateaus exhibit remarkable temperature independence up to 20K, while the quantum oscillations persist up to 75K. This characteristic is clearly shown in Fig. 2d which plots the ρ_{xy} values at 10 and 23 T as a function of temperature. Similar to ρ_{xy} , ρ_{xx} and ρ_{zz} also display temperature independence below 20K under the field of 10 T (Fig. 2h & 2l), but they become temperature dependent under the field of 23 T. In ideal 2D quantum Hall systems, as ρ_{xy} is quantized, ρ_{xx} reaches zero due to the dissipationless transport supported by the chiral

edge state. However, in most practical quantum Hall systems, where bulk states have minor contributions to transport, ρ_{xx} just reaches a minimum as ρ_{xy} exhibits a quantized plateau. In such cases, both ρ_{xx} and ρ_{xy} exhibit temperature independence, attributed to the dominant nonlocal edge transport supported by chiral edge states, which are not subject to backscattering. Conversely, when transport involves substantial bulk contribution, ρ_{xx} and ρ_{xy} become markedly temperature dependent. In stacked quantum Hall systems like BaMnSb_2 , the quantum Hall state is also manifested in the temperature dependence of ρ_{zz} : the temperature independence of ρ_{xx} coincides with the temperature independence of ρ_{zz} , though they show out-of-phase SdH oscillations. Our observation of temperature independence of ρ_{xx} , ρ_{xy} and ρ_{zz} at 10 T are consistent with the quantum Hall state. While not conclusive on its own, this observation motivates the QHE interpretation, for which the key supporting evidence is presented in the following paragraphs. At 23 T, while ρ_{xy} exhibits temperature independent plateau below 20 K (Fig. 2d), both ρ_{xx} and ρ_{zz} exhibit significant temperature dependence even below 20 K (Fig. 2h & 2l), resulting from valley splitting, as discussed below. The QHE signatures seen in Sample #A were also reproduced in another sample #C, (see Supplementary Note 1 and Supplementary Fig. 1)

A detailed analysis of the ρ_{xy} data at 1.4 K (Fig. 3a) reveals robust evidence for the presence of stacked QHE in BaMnBi_2 . As shown in the inset to Fig. 3a, we first extract the step size of $1/\rho_{xy}$ plateaus, denoted as $1/\rho_{xy}^0$, and plot the normalized quantity ρ_{xy}^0/ρ_{xy} as a function of B_F/B , where B_F is the SdH oscillation frequency. We estimate B_F to be 13 T using ρ_{xx} data (Fig. 2g) considering the valleys at 8.4 T and 23.7 T for the temperature above 15 K, where the valley splitting vanishes. Near the minima of ρ_{xx} , ρ_{xy}^0/ρ_{xy} is quantized to half integer values $(\frac{1}{2}, \frac{3}{2})$ corresponding to the half-integer normalized filling factor $(\frac{1}{2}, \frac{3}{2})$ given by B_F/B at the ρ_{xx} minima. The half-integer filling factor corresponds to the non-trivial Berry phase accumulated in the cyclotron orbits. These distinct features, combined with the angular independence of ρ_{xy} , ρ_{xx} and ρ_{zz} at 10 T for $\theta < 40^\circ$ (Fig. 2b, 2f & 2j) and their temperature independence below 20 K for $B \perp ab$ (Fig. 2d, 2h & 2l), are indicative of stacked QHE of Dirac fermions, where the 2D Bi conducting layers between the $\text{Ba}-\text{MnBi}_4-\text{Ba}$ insulating slabs act as effective quantum Hall layers. Although previous

magnetotransport studies on BaMnBi₂ revealed SdH oscillations and its Dirac Fermion transport properties [21,25], its QHE was not demonstrated. Given that the quantum oscillation frequency is proportional to the extremal cross-section area of the Fermi surface, our observed small oscillation frequency (13 T for Sample #A and 11.5 T for sample # B) in BaMnBi₂ suggests that its Dirac band crossing points are positioned very close to the Fermi level.

Similar to the QHE of BaMnSb₂ [20], the bulk QHE of BaMnBi₂ should also originate from the parallel transport of 2D Bi Dirac layers stacked along the c-axis. Hence, the spin valley degeneracy per Bi layer s can be estimated using the equation $\frac{1}{\rho_{xy}^0} = sZ^*(e^2/h)$, where Z^* represents the number of layers per unit length [31]. Given that a unit cell of BaMnBi₂ comprises of two Bi conducting layers, we can simplify the equation to $\frac{1}{\rho_{xy}^0} = s(2/c)(e^2/h)$, where c is the lattice parameter along the out-of-plane direction. Our calculation yielded spin valley degeneracy s to be 3.7. It is important to note that experimentally determined s generally has finite uncertainty due to factors such as inhomogeneous transport caused by dead layers (i.e. those Bi layers not showing QHE), imperfect contacts and/or errors in measuring sample dimensions. With these considerations, we approximate the spin valley degeneracy in BaMnBi₂ to be 4.

Further, we examined the validity of the spin-valley degeneracy of 4 by comparing the carrier density estimated from the quantum oscillation frequency B_F with the transport carrier density extracted from the Hall coefficient. According to Luttinger's theorem, the carrier density of a 2D system with a degeneracy of 4 can be expressed as $n_{2D} = 4eB_F/h$, where e is the elemental charge and h is the Planck's constant. Since each unit cell in BaMnBi₂ contains two conducting Bi layers (Fig. 1a), the 3D carrier density can be expressed as $n_{SdH} = n_{2D}/(c/2)$. The estimated n_{SdH} value for the sample used for ρ_{xx} and ρ_{xy} measurements (i.e. sample #A) is $0.92 \times 10^{19} \text{ cm}^{-3}$ which is in good agreement with the carrier density determined by the Hall coefficient ($n_{Hall} \sim 0.69 \times 10^{19} \text{ cm}^{-3}$). This consistency between n_{SdH} and n_{Hall} provides additional support for a degeneracy of 4 in BaMnBi₂. However, as noted earlier, previous band structure calculations predicted four and two spin-polarized valleys near the X and Y points, respectively, as well as four additional valleys near the midpoint of the Γ M line (Fig. 1b, right panel) in BaMnBi₂ [21], suggesting

an expected s value of 10. The discrepancy between theory and experiment is likely due to (i) inhomogeneous bulk transport and/or imperfect contact, as indicated above, or (ii) the actual spin-valley locked state differing from that predicted in Ref [21]. Considering the consistency of the carrier density measured by the SdH oscillations and Hall effect in our experiment, scenario (i) seems less likely. Our observed SdH frequency closely matches the 13 T value reported in Ref. [21], which was attributed to the α Fermi pockets near the Y point, assuming a Fermi level shift of -33 meV. The extracted degeneracy factor of 4 is consistent with the presence of the α pockets predicted by band structure calculations.

From the temperature dependence of SdH oscillations, we also estimated the effective mass of Dirac fermions in BaMnBi₂. According to the LK theory, the oscillatory part of resistivity can be expressed as: $\Delta\rho \propto R_T R_D \cos \left[2\pi \left(\frac{B_F}{B} - \frac{1}{2} + \beta + \delta \right) \right]$, with temperature damping factor, $R_T = \frac{\lambda T}{\sinh(\lambda T)}$ and Dingle damping factor, $R_D = e^{-\lambda T_D}$, where $\lambda = (2\pi^2 k_B m^*)/(\hbar e B)$. $2\pi\beta$ is the Berry phase and T_D is the Dingle temperature. δ is a phase shift, $\delta = 0$ and $\pm 1/8$ for the 2D and 3D systems, respectively. Figure 3b presents the analysis of the quantum oscillation data where we performed a fast Fourier transform (FFT) of the second derivative of ρ_{zz} (see inset) and normalized the FFT amplitude along the dashed line. The temperature dependence of the normalized FFT amplitude can be accurately fitted with R_T to obtain the effective mass of $m^* = 0.027m_0$. Such a small effective mass is a characteristic feature of Dirac fermions. The m^* in BaMnBi₂ is lower than that of YbMnSb₂ ($0.134m_0$) [32], Sr_{1-y}Mn_{1-z}Sb₂ ($0.14m_0$) [33] and comparable to those of CaMnSb₂ (0.05 - $0.06m_0$) [34] and BaMnSb₂ (0.052 - $0.058m_0$) [35].

As shown in Fig. 1e, an extra peak appears in ρ_{xx} near 33T at 1.4K (marked by the arrow) which gradually diminishes as the temperature increases above 10 K (Fig. 2g). Although our field range (< 35 T) does not allow us to resolve the full double-minimum structure reported by Kondo et al. [20], the similarity in temperature evolution suggests that this feature could be related to valley splitting. In conventional electron systems, such splitting in ρ_{xx} minima is often attributed to Zeeman-driven Landau level splitting. However, our c-axis conductivity σ_{zz} measurements at various tilt angles (Supplementary Fig. S4) show no discernible angular dependence, making a large Zeeman contribution unlikely. If the feature were Zeeman-

induced, the effective g -factor would need to be on the order of 10–20, large enough to produce a strong angular dependence in σ_{zz} — which we do not observe. Given the structural similarity between BaMnBi₂ and BaMnSb₂, we suggest that the observed feature may arise instead from a second-order q -quadratic term [20], similar to what has been observed in BaMnSb₂, which can lift the spin-valley degeneracy and produce valley splitting.

B. Nonlinear Hall measurements

The spin-valley locking model discussed above for BaMnBi₂ is further supported by our nonlinear Hall effect (NLHE) measurements. NLHE refers to a phenomenon where a longitudinal AC current (I^ω) can induce a second-order Hall voltage ($V_\perp^{2\omega}$) along the transverse direction under the time-reversal symmetry condition, with $V_\perp^{2\omega}$ scaling quadratically with I^ω [36]. NLHE can have either intrinsic or extrinsic origins. The intrinsic origin is tied to the quantum geometry of the electron wave function. Theoretical predictions suggest that intrinsic NLHE occurs when electronic bands exhibit a net Berry curvature dipole (BCD) [37] or quantum metric [38,39], which correspond to the imaginary and real parts of the quantum geometric tensor, respectively. BCD-induced NLHE is typically expected in non-centrosymmetric materials with tilted Dirac/Weyl cones [37], while quantum metric-induced NLHE appears in magnetic materials that break both inversion symmetry (P) and time-reversal symmetry (T), with or without PT symmetry [38,39]. BCD-induced NLHE has been observed in various 2D systems, including few-layer WTe₂ [36,40], engineered bilayer graphene [41], and strained or twisted WSe₂ monolayers [42,43]. In 3D materials, related responses have been observed in BaMnSb₂ [26], Dirac/Weyl semimetals [44], and polar Weyl systems such as TaIrTe₄ [45]. Extrinsic NLHE can result from skew scattering and/or side-jump mechanisms in non-centrosymmetric materials [46,47], or from geometric asymmetric scattering due to textured nanoparticles [48].

Similar to BaMnSb₂ [26], BaMnBi₂ is expected to exhibit valley-contrasting Berry curvature due to its spin-valley locked Dirac cones, leading to a net BCD. Therefore, an intrinsic NLHE is expected for BaMnBi₂. To test this, we performed nonlinear transport measurements using lock-in techniques. Our

results showed clear second-harmonic Hall voltage ($V_{\perp}^{2\omega}$) responses driven by alternating currents (Fig. 4a). The measured $V_{\perp}^{2\omega}$ displayed no frequency dependence up to 1800 Hz (Supplementary Fig. 5) and scaled quadratically with the applied current I^{ω} in the current range below 5 mA at 2 K (Fig. 4b), which is consistent with NLHE behavior. Furthermore, as shown in Fig. 4a, the second-harmonic Hall voltage reversed its sign when both the current direction and the Hall probe were simultaneously reversed, aligning with the expected characteristics of NLHE [40].

Another hallmark of BCD-induced NLHE is the nonlinear angle θ_{NLHE} of 90° , θ_{NLHE} is defined as $\arctan(V_{\perp}^{2\omega}/V_{//}^{2\omega})$, where $V_{\perp}^{2\omega}$ represents the nonlinear Hall voltage and $V_{//}^{2\omega}$ the longitudinal voltage. As $V_{//}^{2\omega} = 0$, $\theta_{NLHE} = 90^{\circ}$; that is, the second order response is present only along the transverse direction. Based on the $V_{\perp}^{2\omega}$ and $V_{//}^{2\omega}$ data presented in Fig. 4a, θ_{NLHE} is estimated to be 74° , only 16° deviation from the value of 90° in the ideal geometry. This deviation can be attributed to a small longitudinal second-harmonic signal caused by geometric mixing, as seen in Fig. 4(a), caused by the finite device aspect ratio and unavoidable misalignment between voltage probes and crystallographic axes. This type of mixing is often seen in nonlinear transport measurements and has also been reported in other materials [45]. The second-harmonic Hall voltage increases steadily as the temperature decreases (see Supplementary Fig. 9a), reaching 0.6 μ V at 2K. Notably, the second-harmonic signal remains detectable even at room temperature (300K) (Supplementary Fig. 10), though it is substantially smaller. A stronger room-temperature NLHE might be achieved by optimizing the sample domain and increasing the current density, as discussed later. The quadratic current-voltage characteristic and its frequency independence, as well as the near- 90° nonlinear angle indicate that our observed 2nd order response in BaMnBi₂ is not likely due to extrinsic effects such as junction or thermoelectric effects but has intrinsic BCD contribution (see Supplementary Note 3 for detailed discussions). To further substantiate the intrinsic origin, we not only reproduced the NLHE phenomenon in another sample (see Supplementary Fig. 6), but also found the scaling analysis of the nonlinear Hall conductivity ($\sigma_{yx}^{(2)}$) is aligned with the expected behavior of BCD induced nonlinear

Hall effect, i.e. $\sigma_{yx}^{(2)}$ is approximately proportional to longitudinal conductivity σ_{xx} (see Supplementary Note 3).

Both BaMnSb_2 and BaMnBi_2 exhibit antiferromagnetic order due to Mn moments. Prior transport and band-structure studies indicate, however, that the Mn magnetism only weakly perturbs the low-energy Dirac bands: neither the Fermi surface nor the resistivity show a clear anomaly at the Néel temperature $T_N \approx 288\text{K}$. In BaMnX_2 ($\text{X} = \text{Bi, Sb}$), the spin–valley-coupled Dirac states near E_F are primarily controlled by spin–orbit coupling on the Bi/Sb p -orbitals [49] and the polar lattice distortion [21], rather than by a strong exchange field from the Mn sublattice. For our analysis of the NLHE, we therefore neglect the small influence of the AFM order on the Dirac bands and treat BaMnBi_2 as effectively time-reversal symmetric. This treatment is consistent with our measurements; the nonlinear Hall response shows no anomaly across T_N and the NLHE varies smoothly through T_N , confirming that the magnetic order does not play a role in the Berry-curvature–related physics probed in our study. BaMnSb_2 also shows a similar behavior, as discussed in our prior work [26].

While the second harmonic Hall signal at 10K follows the expected quadratic behavior characteristic of NLHE, the signal at 2 K begins to deviate from this quadratic trend above 5mA as noted above (Fig. 4b). This cannot be attributable to the heating effect in the sample, since the first harmonic signal measurements (inset to Fig. 4b) are linear; the resistance remains unchanged up to 10mA input current. The data is well fitted by incorporating a fourth-order correction, as illustrated by the black fitted curve in Fig 4b. This fourth order term can be associated with high-order nonlinear response [50,51]. Theory demonstrates that the transverse electric field from the nonlinear Hall effect influences the longitudinal conductivity through a bulk electric field effect, that could result in additional fourth order term in transverse direction with respect to applied current [50].

It is important to highlight that the NLHE of BaMnBi_2 is significantly suppressed by the presence of 90° and 180° domains. Note that the sample used in our current measurements has dimensions of 1-2 mm which includes numerous domains (see the image of our device in supplementary Fig. 8). According

to theory [37], for a polar material, maximum nonlinear signal is generated when a current is applied perpendicular to the in-plane polar axis, while no signal is observed when the current is parallel to the polar axis. This means that 90° domains contribute no nonlinear signal, while 180° domains cancel out the overall NLHE signal. Consequently, the NLHE in BaMnBi₂ is diminished, as we observe numerous twin domains through a polarized microscope, with lengths on the order of 10 μm (Fig. 1c). The domain sizes are small in BaMnBi₂ because the orthorhombicity of the crystal structure is small. Finally, it should be noted that the second order nonlinear response is quadratically dependent on the current density. Consequently, samples with smaller cross section areas are more favorable for observing a significant nonlinear signal. In our measurements, we used devices with thickness of around 100 μm which explains the need for high current to extract observable nonlinear signals. For future studies, microscale or thin film devices on a single domain in BaMnBi₂ would be anticipated to significantly enhance the nonlinear signal by several orders of magnitude. This approach holds promises for advancing the exploration of nonlinear phenomena and potential applications, such as terahertz detection and energy harvesting, in BaMnBi₂-based devices.

IV. CONCLUSION

In summary, we observed both bulk QHE and NLHE in the layered Dirac material BaMnBi₂. Our analysis of the QHE revealed a spin-valley degeneracy of 4. Additionally, we identified an intrinsic contribution to the NLHE, indicating that the Dirac bands exhibit a Berry curvature dipole. This finding aligns with theoretical predictions that BaMnBi₂'s electronic structure features valley-dependent spin polarization [21]. This spin-valley locked state contrasts with that of BaMnSb₂, which features spin-polarized valleys near the X point and a degeneracy of 2. These results underscore BaMnBi₂ as a distinctive candidate for exploring spin-valley coupled physics in bulk materials and for potential electronic device applications that leverage both spin and valley degrees of freedom with topological protection.

ACKNOWLEDGEMENTS

This work is supported by the U.S. National Science Foundation (NSF) under award No. DMR-2211327.

L. Min and Z.Q.M. also acknowledge the partial support from NSF through the Materials Research Science and Engineering Center DMR 2011839 (2020 - 2026). The work at the National High Magnetic Field Laboratory is supported by the NSF Cooperative Agreement No. DMR1157490 and the State of Florida. Y.D.G. acknowledges the support by the US Department of Energy under grants DE-SC0019068 for performing high-field transport measurements at the National High Magnetic Field Lab.

References:

- [1] D. Xiao, G.-B. Liu, W. Feng, X. Xu, and W. Yao, Coupled Spin and Valley Physics in Monolayers of MoS₂ and Other Group-VI Dichalcogenides, *Phys. Rev. Lett.* **108**, 196802 (2012).
- [2] J.-X. Li, W.-Q. Li, S.-H. Hung, P.-L. Chen, Y.-C. Yang, T.-Y. Chang, P.-W. Chiu, H.-T. Jeng, and C.-H. Liu, Electric control of valley polarization in monolayer WSe₂ using a van der Waals magnet, *Nat. Nanotechnol.* **17**, 721 (2022).
- [3] K. L. Seyler et al., Valley Manipulation by Optically Tuning the Magnetic Proximity Effect in WSe₂/CrI₃ Heterostructures, *Nano Lett.* **18**, 3823 (2018).
- [4] K. F. Mak, D. Xiao, and J. Shan, Light–valley interactions in 2D semiconductors, *Nat. Photonics* **12**, 451 (2018).
- [5] T. Ye, Y. Li, J. Li, H. Shen, J. Ren, C.-Z. Ning, and D. Li, Nonvolatile electrical switching of optical and valleytronic properties of interlayer excitons, *Light Sci. Appl.* **11**, 23 (2022).
- [6] J. R. Schaibley, H. Yu, G. Clark, P. Rivera, J. S. Ross, K. L. Seyler, W. Yao, and X. Xu, Valleytronics in 2D materials, *Nat. Rev. Mater.* **1**, 16055 (2016).
- [7] K. F. Mak, K. He, J. Shan, and T. F. Heinz, Control of valley polarization in monolayer MoS₂ by optical helicity, *Nat. Nanotechnol.* **7**, 494 (2012).
- [8] H. Zeng, J. Dai, W. Yao, D. Xiao, and X. Cui, Valley polarization in MoS₂ monolayers by optical pumping, *Nat. Nanotechnol.* **7**, 490 (2012).
- [9] X. Xu, W. Yao, D. Xiao, and T. F. Heinz, Spin and pseudospins in layered transition metal dichalcogenides, *Nat. Phys.* **10**, 343 (2014).
- [10] G. Aivazian, Z. Gong, A. M. Jones, R.-L. Chu, J. Yan, D. G. Mandrus, C. Zhang, D. Cobden, W. Yao, and X. Xu, Magnetic control of valley pseudospin in monolayer WSe₂, *Nat. Phys.* **11**, 148 (2015).
- [11] T. Cao et al., Valley-selective circular dichroism of monolayer molybdenum disulphide, *Nat. Commun.* **3**, 887 (2012).
- [12] S. Wu et al., Electrical tuning of valley magnetic moment through symmetry control in bilayer MoS₂, *Nat. Phys.* **9**, 149 (2013).
- [13] R. Wakatsuki, Y. Saito, S. Hoshino, Y. M. Itahashi, T. Ideue, M. Ezawa, Y. Iwasa, and N. Nagaosa, Nonreciprocal charge transport in noncentrosymmetric superconductors, *Sci. Adv.* **3**, e1602390 (2017).
- [14] K. F. Mak, K. L. McGill, J. Park, and P. L. McEuen, The valley Hall effect in MoS₂ transistors, *Science* **344**, 1489 (2014).
- [15] M. Onga, Y. Zhang, T. Ideue, and Y. Iwasa, Exciton Hall effect in monolayer MoS₂, *Nat. Mater.* **16**, 1193 (2017).
- [16] R. Suzuki et al., Valley-dependent spin polarization in bulk MoS₂ with broken inversion symmetry, *Nat. Nanotechnol.* **9**, 611 (2014).
- [17] L. Bawden et al., Spin–valley locking in the normal state of a transition-metal dichalcogenide superconductor, *Nat. Commun.* **7**, 11711 (2016).
- [18] J. Y. Liu et al., Spin-valley locking and bulk quantum Hall effect in a noncentrosymmetric Dirac semimetal BaMnSb₂, *Nat. Commun.* **12**, 4062 (2021).
- [19] S. Huang, J. Kim, W. A. Shelton, E. W. Plummer, and R. Jin, Nontrivial Berry phase in magnetic BaMnSb₂ semimetal, *Proc. Natl. Acad. Sci.* **114**, 6256 (2017).
- [20] H. Sakai et al., Bulk quantum Hall effect of spin-valley coupled Dirac fermions in the polar antiferromagnet BaMnSb₂, *Phys Rev B* **101**, 081104 (2020).
- [21] M. Kondo et al., Tunable spin-valley coupling in layered polar Dirac metals, *Commun. Mater.* **2**, 49 (2021).

[22] Z. Z. Du, H.-Z. Lu, and X. C. Xie, Nonlinear Hall effects, *Nat. Rev. Phys.* **3**, 744 (2021).

[23] Y. Zhang, Y. Sun, and B. Yan, Berry curvature dipole in Weyl semimetal materials: An ab initio study, *Phys Rev B* **97**, 041101 (2018).

[24] C. Ortix, Nonlinear Hall Effect with Time-Reversal Symmetry: Theory and Material Realizations, *Adv. Quantum Technol.* **4**, 2100056 (2021).

[25] L. Li, K. Wang, D. Graf, L. Wang, A. Wang, and C. Petrovic, Electron-hole asymmetry, Dirac fermions, and quantum magnetoresistance in BaMnBi₂, *Phys Rev B* **93**, 115141 (2016).

[26] L. Min et al., Strong room-temperature bulk nonlinear Hall effect in a spin-valley locked Dirac material, *Nat. Commun.* **14**, 364 (2023).

[27] D. Shoenberg, *Magnetic Oscillations in Metals* (Cambridge university press, 2009).

[28] I. M. Lifshits and A. M. Kosevich, On the Theory of Magnetic Susceptibility of Metals at Low Temperatures, *Ukr. J. Phys.* **53**, 112 (2008).

[29] See Supplemental Material at [URL will be inserted by publisher] for more details of quantum Hall effect in additional sample, discussion on origin of nonlinear Hall effect for BaMnBi₂, which includes Refs. [36 ,38 ,40], (n.d.).

[30] Z. Q. Mao, K. D. Nelson, R. Jin, Y. Liu, and Y. Maeno, Observation of Andreev Surface Bound States in the 3-K Phase Region of Sr₂RuO₄, *Phys Rev Lett* **87**, 037003 (2001).

[31] H. Masuda et al., Quantum Hall effect in a bulk antiferromagnet EuMnBi₂ with magnetically confined two-dimensional Dirac fermions, *Sci. Adv.* **2**, e1501117 (2016).

[32] Y.-Y. Wang, S. Xu, L.-L. Sun, and T.-L. Xia, Quantum oscillations and coherent interlayer transport in a new topological Dirac semimetal candidate YbMnSb₂, *Phys Rev Mater* **2**, 021201 (2018).

[33] J. Y. Liu et al., A magnetic topological semimetal Sr_{1-y}Mn_{1-z}Sb₂ (y, z < 0.1), *Nat. Mater.* **16**, 905 (2017).

[34] J. B. He et al., Quasi-two-dimensional massless Dirac fermions in CaMnSb₂, *Phys. Rev. B* **95**, 045128 (2017).

[35] J. Liu et al., Nearly massless Dirac fermions hosted by Sb square net in BaMnSb₂, *Sci. Rep.* **6**, 30525 (2016).

[36] Q. Ma et al., Observation of the nonlinear Hall effect under time-reversal-symmetric conditions, *Nature* **565**, 337 (2019).

[37] I. Sodemann and L. Fu, Quantum Nonlinear Hall Effect Induced by Berry Curvature Dipole in Time-Reversal Invariant Materials, *Phys Rev Lett* **115**, 216806 (2015).

[38] A. Gao et al., Quantum metric nonlinear Hall effect in a topological antiferromagnetic heterostructure, *Science* **381**, 181 (2023).

[39] N. Wang et al., Quantum-metric-induced nonlinear transport in a topological antiferromagnet, *Nature* **621**, 487 (2023).

[40] K. Kang, T. Li, E. Sohn, J. Shan, and K. F. Mak, Nonlinear anomalous Hall effect in few-layer WTe₂, *Nat. Mater.* **18**, 324 (2019).

[41] S.-C. Ho, C.-H. Chang, Y.-C. Hsieh, S.-T. Lo, B. Huang, T.-H.-Y. Vu, C. Ortix, and T.-M. Chen, Hall effects in artificially corrugated bilayer graphene without breaking time-reversal symmetry, *Nat. Electron.* **4**, 116 (2021).

[42] M.-S. Qin, P.-F. Zhu, X.-G. Ye, W.-Z. Xu, Z.-H. Song, J. Liang, K. Liu, and Z.-M. Liao, Strain Tunable Berry Curvature Dipole, Orbital Magnetization and Nonlinear Hall Effect in WSe₂ Monolayer, *Chin. Phys. Lett.* **38**, 017301 (2021).

- [43] M. Huang et al., Giant nonlinear Hall effect in twisted bilayer WSe₂, *Natl. Sci. Rev.* **10**, nwac232 (2022).
- [44] O. O. Shvetsov, V. D. Esin, A. V. Timonina, N. N. Kolesnikov, and E. V. Deviatov, Nonlinear Hall Effect in Three-Dimensional Weyl and Dirac Semimetals, *JETP Lett.* **109**, 715 (2019).
- [45] D. Kumar, C.-H. Hsu, R. Sharma, T.-R. Chang, P. Yu, J. Wang, G. Eda, G. Liang, and H. Yang, Room-temperature nonlinear Hall effect and wireless radiofrequency rectification in Weyl semimetal TaIrTe₄, *Nat. Nanotechnol.* **16**, 421 (2021).
- [46] Z. Z. Du, C. M. Wang, H.-P. Sun, H.-Z. Lu, and X. C. Xie, Quantum theory of the nonlinear Hall effect, *Nat. Commun.* **12**, 5038 (2021).
- [47] A. Tiwari et al., Giant c-axis nonlinear anomalous Hall effect in T_d-MoTe₂ and WTe₂, *Nat. Commun.* **12**, 2049 (2021).
- [48] L. Min et al., Colossal room-temperature non-reciprocal Hall effect, *Nat. Mater.* **23**, 1671 (2024).
- [49] H. Ryu, S. Y. Park, L. Li, W. Ren, J. B. Neaton, C. Petrovic, C. Hwang, and S.-K. Mo, Anisotropic Dirac Fermions in BaMnBi₂ and BaZnBi₂, *Sci. Rep.* **8**, 15322 (2018).
- [50] Y. Onishi and L. Fu, High-efficiency energy harvesting based on a nonlinear Hall rectifier, *Phys Rev B* **110**, 075122 (2024).

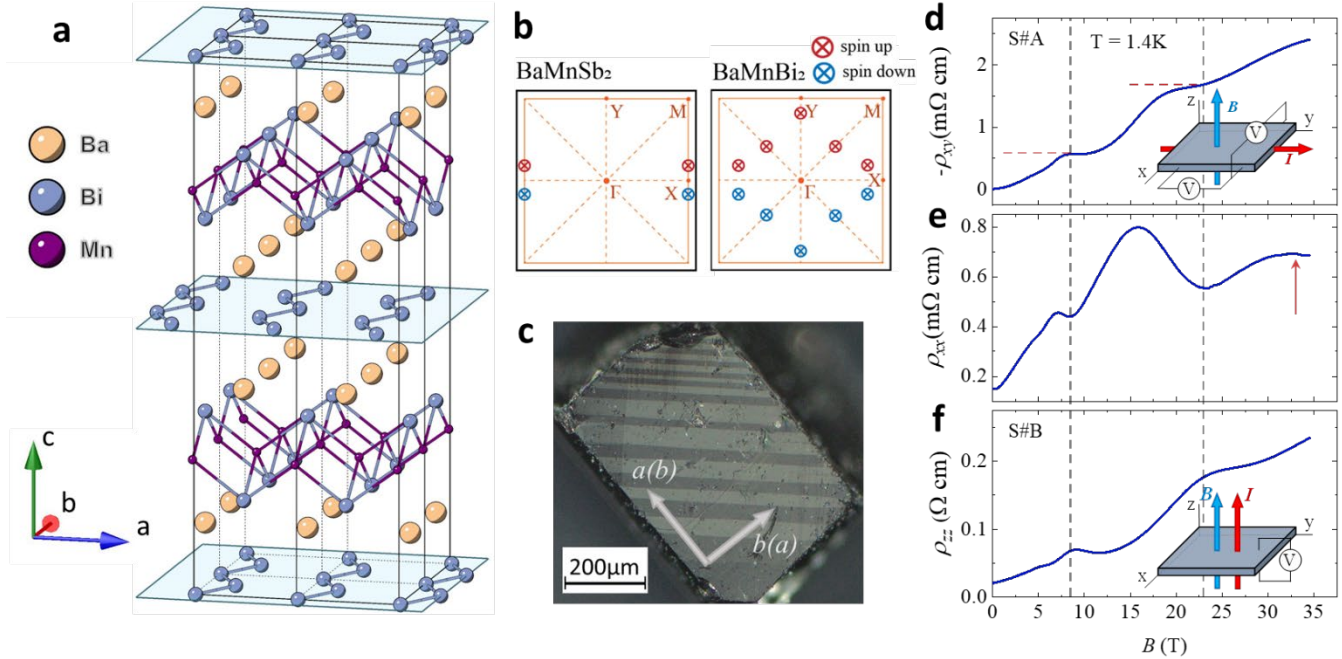


FIG 1. Crystal structure, electronic structure and magnetoresistivity of BaMnBi₂. **(a)** Crystal structure for BaMnBi₂. **(b)** Schematics of Dirac crossing points situated in the Brillouin zone of BaMnBi₂ and BaMnSb₂, as previously reported [18,20,21]. **(c)** The polarized microscope image of the as-grown (001) crystal surface. **(d, e, f)** Hall resistivity (ρ_{xy}), in-plane resistivity (ρ_{xx}), out-of-plane resistivity (ρ_{zz}) vs. magnetic field B up to 35 T at 1.4 K. The inset in **(d)**: schematic of the experimental set-up for the ρ_{xy} and ρ_{xx} measurements on Sample #A (S#A). The inset in **(f)**: schematic sample configuration for the ρ_{zz} measurements on Sample #B (S#B). The dashed lines correspond to quantum Hall states. The arrow in **(e)** shows the local maximum associated with valley splitting.

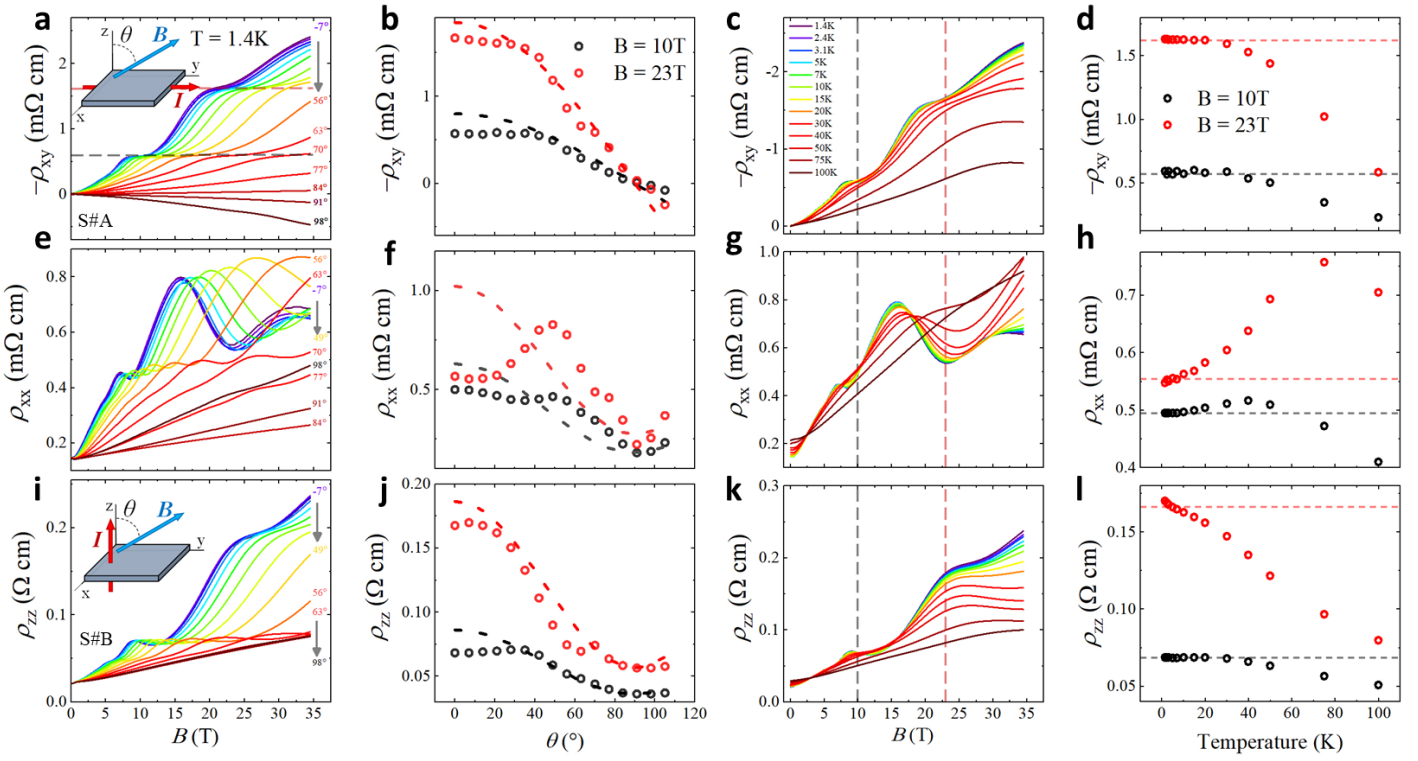


FIG 2. Magnetoresistivity at high fields with different field orientation and temperature. (a, e, i) Angular (θ) dependence of ρ_{xy} , ρ_{xx} and ρ_{zz} vs field B at 1.4 K. Inset in (a & i): Schematic sample configuration for the ρ_{xy} , ρ_{xx} and ρ_{zz} measurements on S#A and S#B. **(b, f, j)** Angular dependence of ρ_{xy} , ρ_{xx} and ρ_{zz} at $B = 10$ T and 23 T. The dashed lines represent the behavior expected for trivial metals. **(c, g, k)** Magnetic field dependence of ρ_{xy} , ρ_{xx} and ρ_{zz} at various temperatures. Dashed lines correspond to the quantum Hall states at $B = 10$ T and 23 T. **(d, h, l)** Temperature dependence of ρ_{xy} , ρ_{xx} and ρ_{zz} at $B = 10$ T and 23 T.

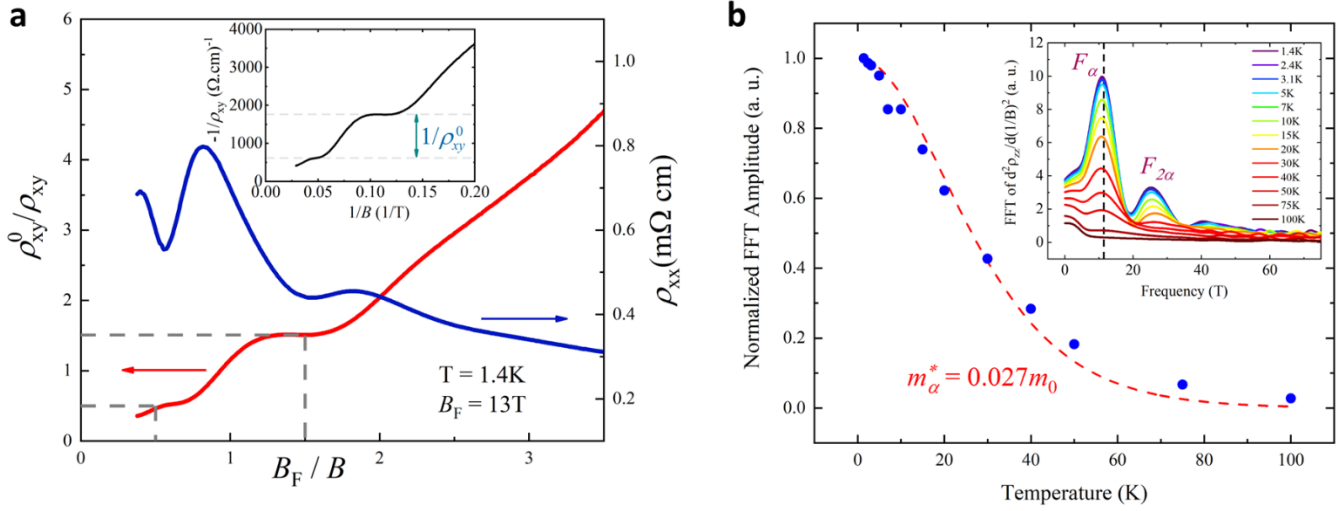


FIG 3. Bulk quantum Hall effect and effective mass analysis based on SdH oscillations. (a) Normalized inverse Hall resistivity (ρ_{xy}^0 / ρ_{xy}) and in-plane resistivity (ρ_{xx}) vs B_F/B at 1.4K. The inset shows the $-1/\rho_{xy}$ as a function of $1/B$. $1/\rho_{xy}^0$ is determined by the vertical interval between steps. (b) Temperature dependence of normalized FFT amplitudes fitted to the LK formula. The inset shows the spectra of the FFT of second derivatives of ρ_{zz} with respect to $1/B$ at various temperatures for S#B. The dashed line represents the first harmonic peak at which the FFT was normalized for the fitting.

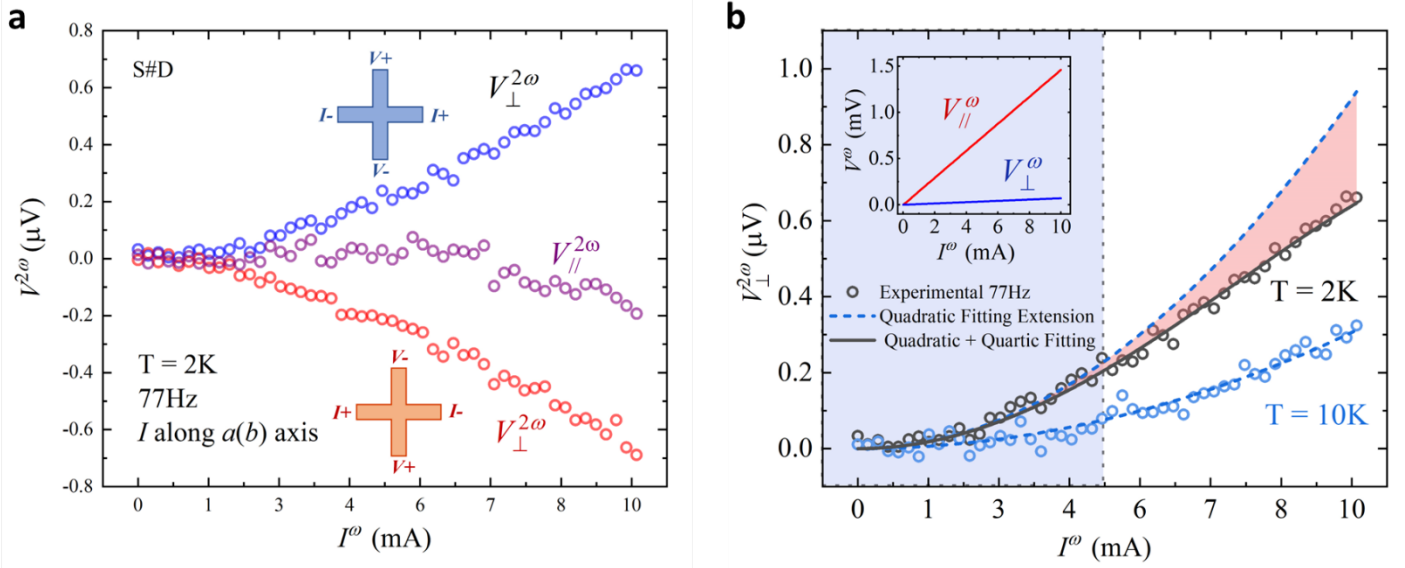


FIG 4. Nonlinear Hall effect in BaMnBi₂. (a) The second harmonic Hall voltage $V_{\perp}^{2\omega}$ vs the input AC current at 2 K. $V_{\parallel}^{2\omega}$ represents the second harmonic longitudinal voltage. The schematics show the current and voltage leads configurations. When the current and voltage leads are reversed simultaneously, the second-harmonic Hall voltage changes sign. (b) $V_{\perp}^{2\omega}$ vs I^{ω} at 77.77 Hz frequency at 2 K and 10 K. The dotted curve shows the quadratic fits, and the solid black curve shows quadratic + quartic fit. The blue shaded region shows the region where quadratic curve well fits the $V_{\perp}^{2\omega}$ data for 2 K. The inset shows first harmonic longitudinal and transverse voltage vs the input current at 2 K.